



RESEARCH LETTER

10.1002/2016GL071990

Key Points:

- Black smoker heat flux may be related to magma recharge
- Seismogenic cracking induced by magma recharge may enhance crustal permeability
- Crustal permeability may be further modified by cracking induced by dike propagation and tectonic faulting

Supporting Information:

- Supporting Information S1

Correspondence to:

G. M. Arnoux,
arnoux@uoregon.edu

Citation:

Arnoux, G. M., D. R. Toomey, E. E. E. Hooft, W. S. D. Wilcock, J. Morgan, M. Warner, and B. P. VanderBeek (2017), Seismic evidence that black smoker heat flux is influenced by localized magma replenishment and associated increases in crustal permeability, *Geophys. Res. Lett.*, *44*, 1687–1695, doi:10.1002/2016GL071990.

Received 11 JUL 2016

Accepted 20 JAN 2017

Accepted article online 24 JAN 2017

Published online 16 FEB 2017

Seismic evidence that black smoker heat flux is influenced by localized magma replenishment and associated increases in crustal permeability

Gillean M. Arnoux¹ , Douglas R. Toomey¹ , Emilie E. E. Hooft¹ , William S. D. Wilcock² , Joanna Morgan³ , Mike Warner³, and Brandon P. VanderBeek¹ 

¹Department of Earth Sciences, University of Oregon, Eugene, Oregon, USA, ²School of Oceanography, University of Washington, Seattle, Washington, USA, ³Department of Earth Sciences and Engineering, Imperial College London, London, UK

Abstract Hydrothermal circulation at mid-ocean ridges is responsible for ~25% of Earth's heat flux and controls the thermal and chemical evolution of young oceanic crust. The heat flux of black smoker hydrothermal systems is thought to be primarily controlled by localized magma supply and crustal permeability. Nevertheless, magma chamber characteristics and the nature of crustal permeability beneath such systems remain unclear. Here we apply three-dimensional full-waveform inversion to seismic data from the hydrothermally active Endeavour segment of the Juan de Fuca Ridge to image the upper crust in high resolution. We resolve velocity variations directly above the axial magma chamber that correlate with variations in seismicity, black smoker heat flux, and the depth of the axial magmatic system. We conclude that localized magma recharge to the axial magma lens, along with induced seismogenic cracking and increased permeability, influences black smoker heat flux.

1. Introduction

Much of what we know regarding heat flux between magmatic and hydrothermal systems at mid-ocean ridges stems from modeling. Models of hydrothermal flow, in combination with field observations, indicate sites of vigorous hydrothermal circulation overlie portions of the axial magma chamber (AMC) that have undergone recent magma replenishment [Singh *et al.*, 1999; Humphris and Cann, 2000; Liu and Lowell, 2009; Wilcock *et al.*, 2009]; such replenishment events maintain the heat necessary to sustain the observed long-term heat fluxes of black smoker hydrothermal systems [Liu and Lowell, 2009]. However, seismic observations and more recent hydrothermal modeling indicate black smoker heat flux is controlled not only by localized magma supply rates but also by a heterogeneous crustal permeability structure [Wilcock *et al.*, 2009; Lowell *et al.*, 2013; Singh *et al.*, 2013]. Realistic estimates of crustal permeability beneath black smoker vent fields are thus necessary to better understand these systems [Lowell *et al.*, 2013]. Three-dimensional full-waveform inversion (FWI) [Warner *et al.*, 2013], an advanced seismic imaging technique commonly applied to industry data sets, has the resolution necessary to constrain fine-scale velocity structure that can be used to infer relative spatial variations in crustal permeability [Carlson, 2011].

Here we apply three-dimensional FWI to seismic data collected on the Endeavour segment of the Juan de Fuca Ridge to develop high-resolution images of the magmatic-hydrothermal reaction zone—the region near the magmatic heat source in which high-temperature, water-rock reactions occur—beneath several well-studied hydrothermal vent fields. The central rift valley of the Endeavour segment hosts five long-lived black smoker vent fields (from north to south—Sasquatch, Salty Dawg, High Rise, Main Endeavour, and Mothra) driven by heat loss from an AMC located approximately 2.1–3.3 km below the seafloor [Van Ark *et al.*, 2007; Carbotte *et al.*, 2008, 2012] (Figure 1). These vent fields are characterized by large variations in heat flux [Thompson *et al.*, 2005; Kellogg, 2011], steep gradients in temperature and chemistry [Butterfield *et al.*, 1994; Kelley *et al.*, 2002, 2012], and high levels of associated seismicity [Wilcock *et al.*, 2009; Kelley *et al.*, 2012]. We resolve fine-scale velocity variations within the magmatic-hydrothermal reaction zone that correlate with concentrations of seismicity, the heat fluxes of the overlying hydrothermal vent fields, and variations in the axial magmatic system. In conjunction with previous microseismicity and hydrothermal studies, we conclude that black smoker heat flux is influenced by localized magma replenishment to the AMC, which induces seismogenic cracking and increases crustal permeability within the overlying reaction zone. The

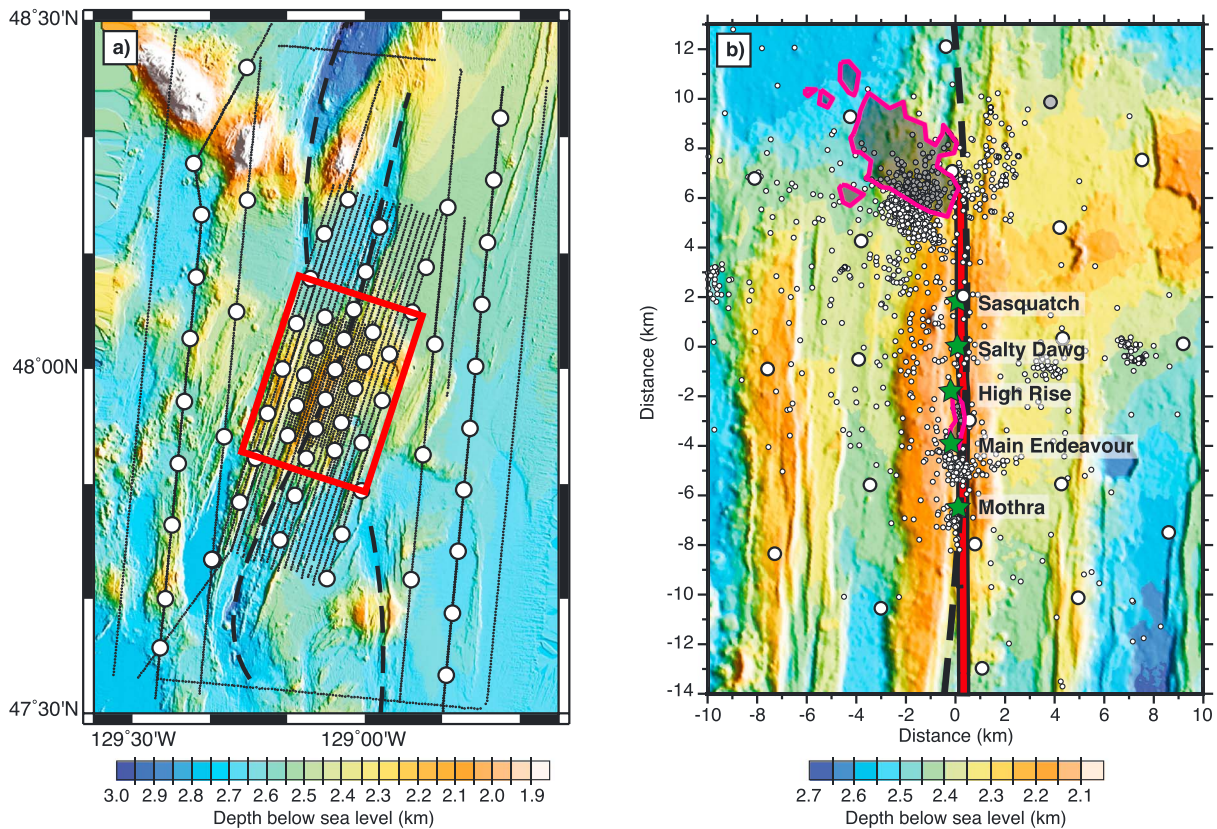


Figure 1. The Endeavour seismic tomography (ETOMO) experiment. (a) Configuration of the ETOMO experiment conducted along the Endeavour segment of the Juan de Fuca Ridge. Seismic data were collected using four-component ocean bottom seismometers (OBSs; large white circles) and the 6600 cubic inch air gun array of the R/V *Marcus G. Langseth*. Black dots show shot locations, and thick dashed lines indicate the plate boundary. Data from the crustal grid (red box) were used in FWI. (b) Crustal grid of the ETOMO experiment consisting of 22 OBSs (large white circles) that recorded 1673 air gun shots; one OBS did not record data (grey circle). Vent fields (green stars) and axial magma chamber (AMC) reflector (red line) [Van Ark et al., 2007] are overlaid. Magenta contours show areas with earthquake densities >20 events per square kilometer recorded during the February 2005 swarm [Hooft et al., 2010]. Small white circles are epicenters of post-swarm earthquakes that occurred between October 2005 and June 2006 [Weekly et al., 2013].

interplay between these linked processes and the clogging of permeability by hydrothermal deposits gives rise to an evolving, strongly heterogeneous permeability structure within the magmatic-hydrothermal reaction zone along the segment.

2. Experiment and Methods

2.1. Endeavour Tomography Experiment

The Endeavour tomography (ETOMO) experiment was conducted in 2009 on the Endeavour segment and used a seismic array consisting of 68 four-component (three orthogonal geophones and one hydrophone) ocean bottom seismometers (OBSs) to record ~5500 air gun shots from the 36-element, 6600 cubic inch air gun array of the R/V *Marcus G. Langseth* [Weekly et al., 2014] (Figure 1a). The central portion of the experiment, or the crustal grid, encompassed the five hydrothermal vent fields and recorded seismic data for imaging the detailed structure of the upper crust underlying the hydrothermal vent fields (Figure 1b and red box in Figure 1a). The crustal grid includes 22 OBSs with an average spacing of 5 km that recorded 1673 air gun shots, with spacing of ~450 m along and 450 m to 1 km between each shot line, representing the densest portion of the ETOMO experiment; one OBS within the crustal grid did not record data (grey circle in Figure 1b). We use data from a subset of the crustal grid that consists of a total of ~24,500 seismograms recorded on the hydrophones of 21 OBSs (Figure 1). Examples of the seismic data are provided in Figure S1 in the supporting information.

2.2. Three-Dimensional Full-Waveform Inversion

A previous travel time tomography study provides a three-dimensional starting model of upper crustal P wave velocity and anisotropy [Weekly *et al.*, 2014] (Figures S2a and S3a–S3d). For the purpose of this study, the initial velocity model was constructed such that it incorporated only the crustal grid portion of the ETOMO experiment. FWI requires approximately four grid points per wavelength for the maximum frequency and the minimum velocity, which is approximately 1500 m s^{-1} within the water column [Morgan *et al.*, 2016]. Thus, a grid spacing of 50 m was chosen so that our inversions could reach a maximum frequency of 6.5 Hz. The velocity model is $20 \text{ km} \times 27 \text{ km}$ wide and 8.95 km deep, corresponding to a grid of $401 \times 541 \times 180$ nodes. Reciprocity was applied to reduce the computational cost of the inversions.

The starting velocity model was smoothed relative to the travel time tomography model [Weekly *et al.*, 2014], as it is preferable to start FWI with a smooth model [Morgan *et al.*, 2016]. Smoothing was applied horizontally and vertically over a distance of about half the seismic wavelength at the lowest inversion frequency, 3 Hz, to remove structure below the theoretical resolution of FWI. This effectively smoothed layer 2A, which was included in the travel time tomography model based on thickness estimates from multichannel seismic (MCS) data [Van Ark *et al.*, 2007]. The data were band-pass-filtered between 3 and 6 Hz and windowed around the first arriving crustal refractions (P_g) using a window length of 750 ms. While S waves were infrequently present within this window, as observed on the radial channel, their energy did not contribute to that on the hydrophone (Figure S4).

Data at larger offsets from the OBSs within the crustal grid were dominated by noise (Figures S5a and S6). The adverse effects of noise are frequency dependent, such that data up to 10 km and 15 km offsets were useable in the inversions at low (3–4 Hz) and high (4–6 Hz) frequencies, respectively (Figures S6a and S6b). Furthermore, at offsets closer than approximately 2.9 km, the first arrival is obscured by its interactions with the large amplitude direct arrivals through the water column. Therefore, data between offsets of 2.9–10 km were inverted with 10 iterations at low-pass cutoff frequencies of 3.0, 3.4, and 3.9 Hz. Data at offsets between 2.9 and 15 km were then input into the inversion and 5 iterations performed at 3.3 and 3.8 Hz, followed by 10 iterations performed at 4.4 and 5.1 Hz. During FWI, velocity is iteratively updated whereas anisotropy is held constant [Morgan *et al.*, 2016]; examples of V_p model updates during the inversion are shown in Figure S7 in the supporting information. A more detailed description of the methods is provided in Morgan *et al.* [2016].

3. Results

Figures S2 and S3 in the supporting information show comparisons between the travel time tomography and FWI results. While generally consistent with results from travel time tomography [Weekly *et al.*, 2014], our FWI images depict larger-amplitude anomalies and provide improved spatial resolution of the crust above the axial magmatic system and beneath the active vent fields (Figures 2 and 3). Synthetic resolution tests indicate the ability to resolve structure on the order of $0.8\text{--}1 \text{ km}^3$ within the upper 3 km of crust, representing a four-fold improvement over the travel time tomography results [Weekly *et al.*, 2014] (see supporting information; Figures S8 and S9). Resolution decreases with depth, however, such that structures on the order of 1.5 km^3 are better constrained down to 2.5 km below seafloor (bsf) but are unrecoverable below 3 km. We therefore avoid structural interpretations below 3 km bsf (see supporting information). Additional information pertaining to model resolution and fitness is provided in the supporting information [Thurber, 1983; Toomey and Foulger, 1989; Toomey *et al.*, 1994].

3.1. Along-Axis Structure

Significant heterogeneity in the velocity structure is observed along axis (Figures 2a and S10). A large low-velocity anomaly is detected 2.5 km bsf, the top of which correlates well with the depth of the AMC reflector [Van Ark *et al.*, 2007; Carbotte *et al.*, 2008] (Figure 2a); the magnitude of this anomaly is greatest between the Main Endeavour and High Rise fields and decreases to the north and south. Directly overlying the AMC reflector, within the inferred location of the magmatic-hydrothermal reaction zone, low-velocity anomalies are resolved beneath Main Endeavour and High Rise, whereas the other vent fields are underlain by higher velocities (Figure 2a); we note, however, that the reaction zone above the AMC is likely much thinner than is resolved by FWI. There is a correlation between the velocity, density of earthquakes, and intensity of hydrothermal venting. The region of the most concentrated seismicity coincides with the low velocities that are

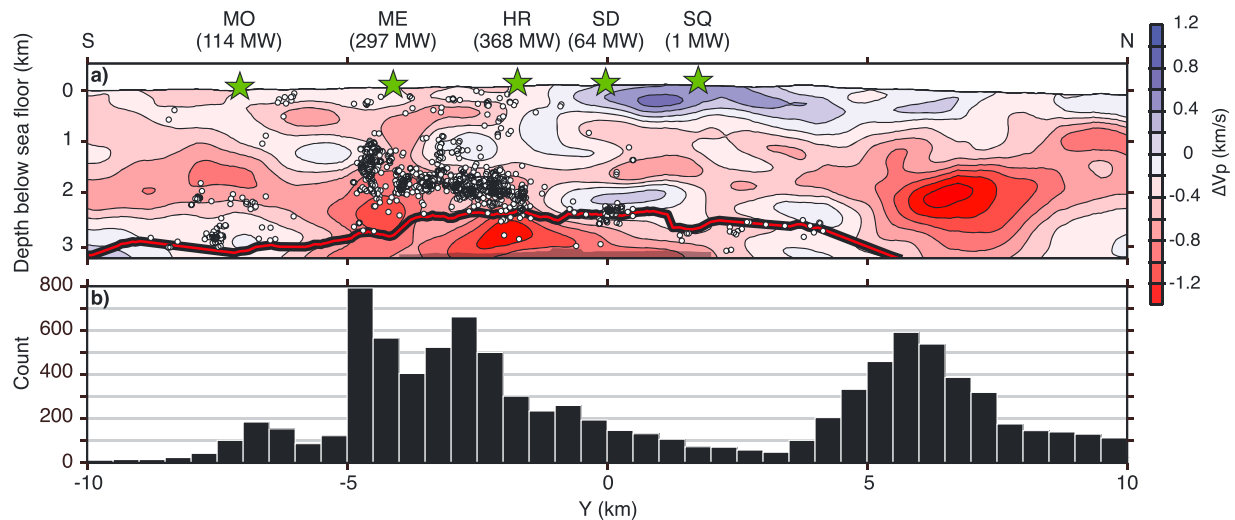


Figure 2. Along-axis section of preferred model and microseismicity. (a) Along-axis section ($X = 0.1$ km, see Figure 1b) of the preferred full-waveform inversion (FWI) model. Three-dimensional velocity anomalies are plotted relative to a horizontal average of the starting model and masked in regions where the derivative weight sum is less than 10 (see supporting information). Section shows the locations of the vent fields (green stars), hypocenters for earthquakes recorded between 2003 and 2004 (white circles) [Wilcock *et al.*, 2009], and AMC reflector (red and black line) [Van Ark *et al.*, 2007]. The position of the AMC was obtained by converting two-way travel times of the AMC [Van Ark *et al.*, 2007] to depth assuming a horizontal average of the velocity model from travel time tomography. The heat fluxes of the five vent fields are provided above each vent [Kellogg, 2011]: MO = Mothra, ME = Main Endeavour, HR = High Rise, SD = Salty Dawg, and SQ = Sasquatch. (b) Histogram of ~6000 earthquakes that occurred within 2 km of the ridge axis, located via an automated method from 2003 to 2006 [Weekly *et al.*, 2013]. Earthquakes are binned in 0.5 km intervals along the ridge axis. Hypocenters from this data set are not shown in Figure 2a because of poor depth constraints since many of these earthquakes occurred outside of the seismic network. Modified from Figure 12c in Weekly *et al.* [2014].

located beneath the Main Endeavour and High Rise fields, which in comparison to the other vent fields on the Endeavour segment are characterized by a larger number of black smoker vents [Kelley *et al.*, 2002], higher maximum venting temperatures [Kelley *et al.*, 2002], and higher heat fluxes [Kellogg, 2011] (Figure 2).

A prominent low-velocity anomaly lies 5 km to the north of the Sasquatch vent field, centered at 2 km bsf in a region of enhanced seismicity (Figures 2 and S11). No reflector corresponding to this low-velocity anomaly was detected in a 2002 MCS study [Van Ark *et al.*, 2007; Carbotte *et al.*, 2008, 2012]. Low-velocity anomalies also underlie Mothra at 1–2 km bsf and extend to the south of the vent fields.

3.2. Across-Axis Structure

FWI results for rise-perpendicular sections located across four of the hydrothermal vent fields—Mothra, Main Endeavour, High Rise, and Salty Dawg—are shown in Figure 3. At 2–3 km bsf, a pronounced low-velocity zone that correlates with the AMC reflector underlies all of the vent fields aside from Mothra, the southernmost field. We note that the width of the midcrustal low-velocity anomaly, at 3 km bsf in Figures 3b–3d, varies between 1 and 2 km in width and is thus greater than the width of the overlying AMC reflector (0.4–1.2 km) [Van Ark *et al.*, 2007; Carbotte *et al.*, 2008, 2012]. Resolution tests indicate that at these depths we can resolve features approximately 1–1.5 km in width (see supporting information), suggesting that a broader low-velocity zone likely underlies the AMC reflector.

Significant low-velocity anomalies are imaged that underlie the abyssal hills within ± 2 km of the ridge axis (Figures 3 and S11), correlating with the approximately 2 km wide region in which <10,700 year old dikes are located [Clague *et al.*, 2014]. Farther off-axis, these low-velocity anomalies give way to high velocities, forming a sequence of alternating low- and high-velocity anomalies that parallel the ridge axis (Figures 3 and S11). The bands have an average width of 2–3 km and span the length of the entire segment within our study area. The widest and largest magnitude high-velocity band is located just east of the westernmost abyssal hill (Figures S11a and S11b).

4. Discussion

Above the AMC reflector, we attribute the observed variations in the velocity structure (Figures 2a and 3) primarily to fluctuations in porosity and, by inference, permeability (Figures S12 and S13). In the upper to

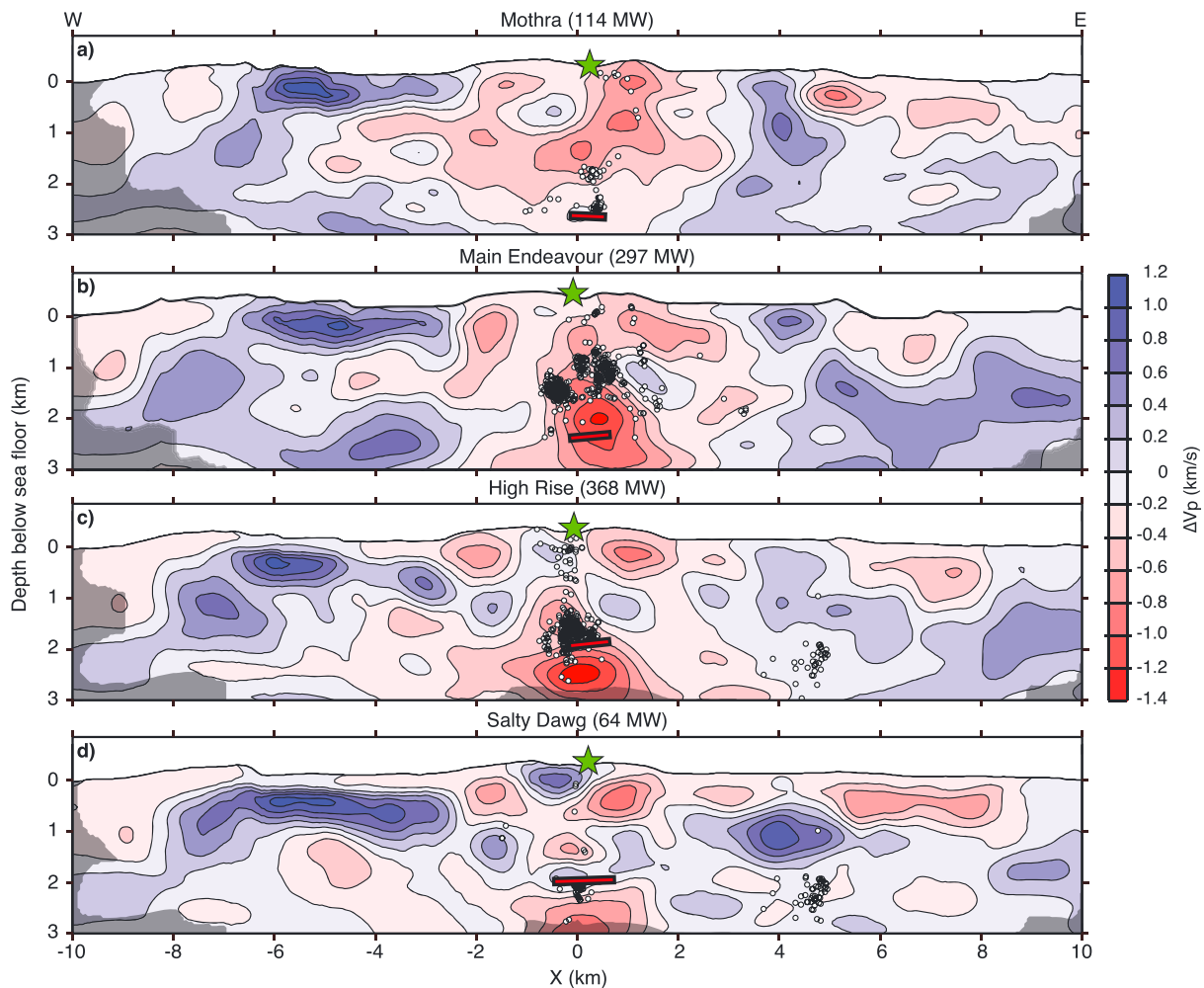


Figure 3. Across-axis sections showing velocity anomalies beneath hydrothermal vent fields. Vertical sections crossing the ridge axis at (a) Mothra ($Y = -7$ km), (b) Main Endeavour ($Y = -4.1$ km), (c) High Rise ($Y = -1.7$ km), and (d) Salty Dawg ($Y = 0$ km), masked in regions where the derivative weight sum is less than 10 (see supporting information). Overlain are the hypocenters for earthquakes recorded between 2003 and 2004 (white circles) [Wilcock *et al.*, 2009], vent field locations (green stars), and the AMC reflector (red and black line) [Van Ark *et al.*, 2007]. Heat fluxes are provided above each vent field [Kellogg, 2011].

middle crust, variations in V_p provide a reliable estimate of crustal porosity [Swift *et al.*, 2008; Carlson, 2010; Carlson, 2014]. We note that subsolidus variations in temperature also affect seismic properties. However, since compressional wave speeds show only a slight linear decrease with increasing temperatures below roughly 600°C [Christensen, 1996; Kern *et al.*, 2001], large lateral variations in V_p above the AMC and within the upper 3 km of oceanic crust are most likely due to localized changes in porosity; in the supporting information, we describe a method to convert absolute velocity to porosity and provide images of the converted velocity structure Equation (S1), Table S1, and Figures S12 and S13). While porosity is not equivalent to crustal scale hydrologic permeability, it is the primary variable that affects permeability [Bernabé *et al.*, 2003] and may therefore be linked to variations in permeability in the upper to middle oceanic crust [Carlson, 2011]. Yet, as there is no simple way to relate porosity and permeability, we relate V_p and porosity to permeability qualitatively.

The low velocities beneath the near-axis abyssal hills are consistent with enhanced porosity along a complex of inward and outward facing normal faults (Figures 3 and 4b). In this model, the complex of outward facing faults are draped by syntectonic lava flows and termed “volcanic-growth faults” [Macdonald *et al.*, 1996]. Crustal damage caused by dike propagation from the AMC to the seafloor may also contribute to the low seismic velocities found beneath the abyssal hills and those forming the v-shaped low-velocity pattern at depth [Delaney *et al.*, 1984; Fontaine *et al.*, 2014]. This interpretation offers an explanation for the occurrence of

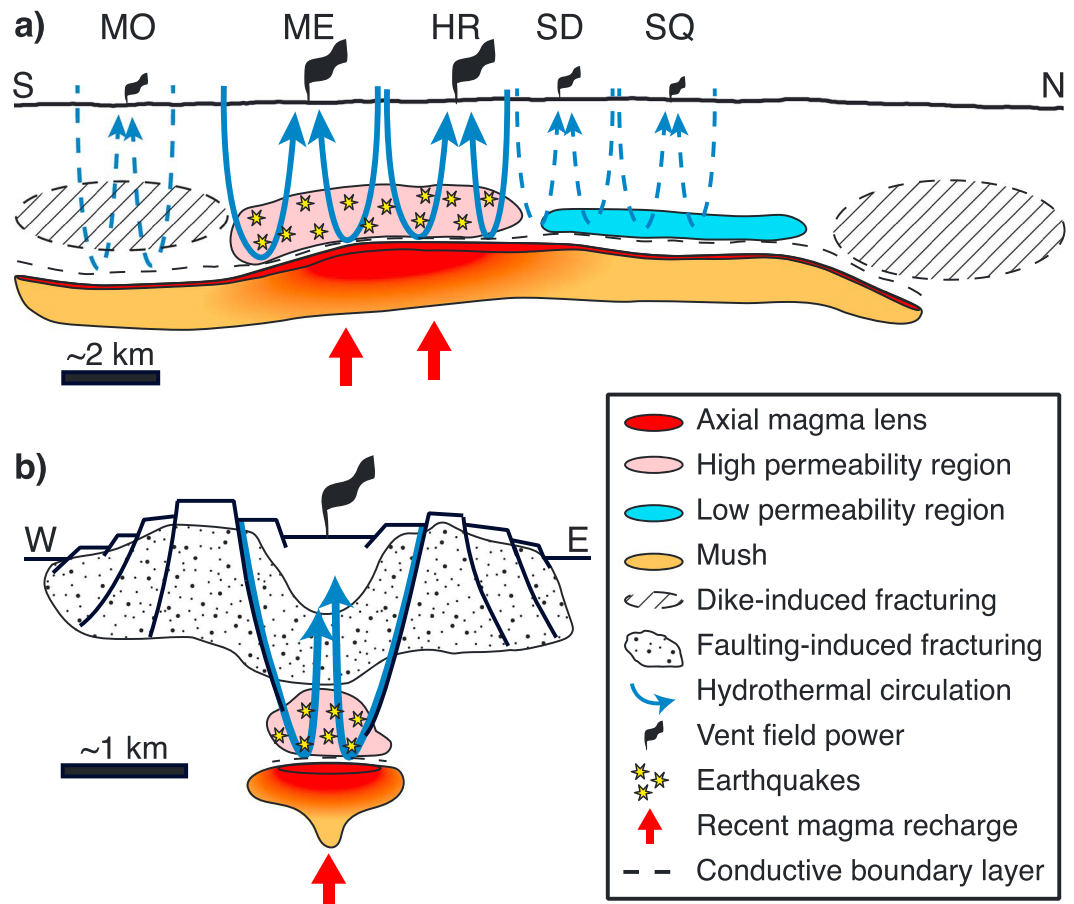


Figure 4. Conceptual illustration for processes that modify crustal permeability. (a) Along-axis section depicting the relations between active processes and vent field power output (stylized black swaths). Recent recharge (red arrows) to the AMC (red lens) induces seismogenic cracking (yellow stars) that enhances crustal permeability (pink region), resulting in a thin conductive boundary layer (dashed line; CBL) and efficient hydrothermal circulation (solid blue arrows). Lack of recent magma replenishment results in a reduction of permeability via hydrothermal clogging within the reaction zone (light blue region) and a thicker CBL, resulting in inefficient hydrothermal circulation (dashed blue arrows) that cannot reach the CBL. Regions of dike-induced fracturing are shown by ellipses with diagonal lines. (b) Rise-perpendicular section showing inward dipping normal faults near the axial valley serve as pathways for hydrothermal fluids, and along with outward facing faults on the abyssal hills, fracture the crust, generating zones of enhanced permeability (stippled regions). Efficient hydrothermal circulation is facilitated by enhanced permeability above the AMC, resulting from seismicity associated with recent magma chamber recharge; this also results in a thin CBL above the AMC. Gradient in mush zone indicates higher melt fractions in red regions.

anomalously young lavas sampled off-axis [Clague *et al.*, 2014]. The alternating sequence of low- and high-velocity anomalies further off-axis appears to be associated with bathymetric highs and lows, with lower velocities centered beneath the outer flanks of the outer abyssal hills. We therefore infer that this banding indicates variations in the thickness of layer 2A, in concert with previous results [Barclay and Wilcock, 2004; Van Ark *et al.*, 2007; Weekly *et al.*, 2014]. Furthermore, we attribute the shallow (1–2 km bsf) low-velocity anomalies beneath and to the south of Mothra and the large low-velocity anomaly north of Sasquatch to fracturing resulting from dike propagation and tectonic fracturing associated with the 6 year nonerupting spreading event that occurred from 1999 to 2005 along the Endeavour segment [Bohnenstiehl *et al.*, 2004; Hooft *et al.*, 2010; Weekly *et al.*, 2013] (Figures 2a and 4a).

Beneath the AMC reflector [Van Ark *et al.*, 2007; Carbotte *et al.*, 2008, 2012], we attribute variations in the magnitude of the midcrustal low-velocity zone to lateral variations in melt content of the axial magmatic system (Figure 4a). Owing to the limited midcrustal data incorporated in the current analysis, the true magnitude of the low-velocity anomaly is underestimated; thus, we cannot place absolute bounds on the melt fraction. However, the observed variation in the magnitude of the velocity anomaly along axis is a resolvable

feature (see supporting information), which allows us to infer that melt fractions in the magmatic system beneath the AMC reflector must vary. Notably, the region of lowest velocities beneath the AMC reflector—and by inference highest melt fractions—coincides with the concentration of seismicity in 2003–2004 between the Main Endeavour and High Rise vent fields, which are characterized by a larger number of black smoker vents [Kelley *et al.*, 2002], higher maximum venting temperatures [Kelley *et al.*, 2002], and higher heat fluxes [Kellogg, 2011] than the other vent fields on the Endeavour segment (Figure 2a). Focal mechanisms for these earthquakes are also consistent with stress perturbations resulting from injection of magma into a sill [Wilcock *et al.*, 2009]. We therefore infer that the observed variation in the low-velocity anomaly beneath the AMC reflector is the result of a more recent magma recharge event between Main Endeavour and High Rise (Figures 2a and 4).

On the basis of the coincident variations in the magmatic system, rates of seismicity, and power output of the overlying vent fields, we infer magma recharge associated with seismogenic cracking and increased permeability exerts a primary control on black smoker heat flux. Black smokers are driven by heat transferred from an axial magma reservoir via a thin (10–100 m) thermal boundary layer (TBL) at the interface between hydrothermal circulation cells and the roof of the magma chamber [Lowell and Germanovich, 2004; Liu and Lowell, 2009]. In the absence of magma replenishment, the TBL thickens owing to hydrothermal clogging [Wilcock and Delaney, 1996] and crystallization of magma to the roof of the reservoir [Singh *et al.*, 1999; Lowell and Germanovich, 2004; Liu and Lowell, 2009]. We infer that the former process is apparent in the relatively high velocities and low rates of seismicity that characterize the reaction zone beneath Mothra, Salty Dawg, and Sasquatch, the vent fields with the lowest heat fluxes on the Endeavour segment (Figures 2a, 3a, 3d, and 4a). Recent magma injection, on the other hand, induces seismogenic cracking that counteracts the thickening of the TBL by increasing crustal permeability within the reaction zone [Wilcock *et al.*, 2009], a scenario evident beneath Main Endeavour and High Rise, the most robust vent fields on the segment (Figures 2a, 3b, 3c, and 4); magma replenishment may also thin the TBL by limiting crystallization on the roof of the reservoir. The absolute time scales for these interconnected effects are unconstrained, though modeling indicates that magmatic perturbations to the AMC may take from months to years to influence heat flux at the surface [Germanovich *et al.*, 2011]; a decrease in magma resupply would take a similar amount of time to result in a decline in seafloor vent temperatures and heat output [Singh *et al.*, 2013; Choi and Lowell, 2015]. In conjunction with previous microseismicity and hydrothermal studies, we conclude the large variations in heat flux that characterize the Endeavour hydrothermal system are a manifestation of localized magma injection that produces an evolving and strongly heterogeneous crustal permeability structure via induced seismogenic cracking.

Acknowledgments

We thank the officers and crew of the R/V *Marcus G. Langseth* as well as the OBS teams from Scripps Institution of Oceanography and Woods Hole Oceanographic Institution for their assistance in the acquisition of the seismic data. Additional assistance was provided by onboard passive acoustic technicians and marine mammal observers to ensure that data collection was accomplished in compliance with guidelines set forth by marine environmental assessments and permits. The experiment and analysis were supported by the National Science Foundation under grants OCE-0454700 to the University of Washington and OCE-0454747, OCE-0651123, and OCE-1634786 to the University of Oregon. Sponsors of the FULLWAVE consortia—BG, BP, Chevron, CGGVeritas, ConocoPhillips, DONG, DownUnder, GeoSolutions, ENI, HESS, Maersk, NExen, PGS, Rio Tinto, Statoil, Sub Salt Solutions, TGS, Tullow Oil, and Woodsite—supported the development of the 3-D full-waveform inversion software used in this study.

5. Conclusions

Previous work has demonstrated the necessity for magma replenishment in maintaining the longevity and high heat fluxes of black smoker hydrothermal systems [Humphris and Cann, 2000; Lowell and Germanovich, 2004; Liu and Lowell, 2009]. While it has been proposed that magma recharge events modify crustal permeability [Wilcock *et al.*, 2009; Lowell *et al.*, 2013], geophysical observations to support this hypothesis have been lacking. Our results imply that magma recharge and induced seismogenic cracking contribute to enhanced crustal permeability and that spatial and temporal variations in this process give rise to an evolving, highly heterogeneous crustal permeability that governs, in part, the heat flux of black smoker hydrothermal systems and the pattern of hydrothermal circulation. Cracking induced by dike propagation and tectonic faulting may also modify crustal permeability, providing additional controls on hydrothermal circulation. Thus, our results support inferences made from modeling studies and provide constraints on spatial variations in the permeability structure of the crust that can be incorporated into models of hydrothermal flow to further our understanding of magma-driven hydrothermal systems.

References

- Barclay, A. H., and W. S. D. Wilcock (2004), Upper crustal seismic velocity structure and microearthquake depths at the Endeavour Segment, Juan de Fuca Ridge, *Geochem. Geophys. Geosyst.*, 5, Q01004, doi:10.1029/2003GC000604.
- Bernabé, Y., U. Mok, and B. Evans (2003), Permeability-porosity relationships in rocks subjected to various evolution processes, *Pure Appl. Geophys.*, 160(5), 937–960, doi:10.1007/PL00012574.
- Bohnenstiehl, D. R., R. P. Dziak, M. Tolstoy, C. G. Fox, and M. Fowler (2004), Temporal and spatial history of the 1999–2000 Endeavour Segment seismic series, Juan de Fuca Ridge, *Geochem. Geophys. Geosyst.*, 5, Q09003, doi:10.1029/2004GC000735.

- Butterfield, D. A., R. E. McDuff, M. J. Mottl, M. D. Lilley, J. E. Lupton, and G. J. Massoth (1994), Gradients in the composition of hydrothermal fluids from the Endeavour segment vent field: Phase separation and brine loss, *J. Geophys. Res.*, *99*(B5), 9561–9583, doi:10.1029/93JB03132.
- Carbotte, S., J. P. Canales, M. Nedimović, H. Carton, and J. Mutter (2012), Recent seismic studies at the East Pacific Rise 8°20′–10°10′N and Endeavour Segment: Insights into mid-ocean ridge hydrothermal and magmatic processes, *Oceanography*, *25*, 100–112, doi:10.5670/oceanog.2012.08.
- Carbotte, S. M., M. R. Nedimović, J. P. Canales, G. M. Kent, A. J. Harding, and M. Marjanović (2008), Variable crustal structure along the Juan de Fuca Ridge: Influence of on-axis hot spots and absolute plate motions, *Geochem. Geophys. Geosyst.*, *9*, Q08001, doi:10.1029/2007GC001922.
- Carlson, R. L. (2010), How crack porosity and shape control seismic velocities in the upper oceanic crust: Modeling downhole logs from Holes 504B and 1256D, *Geochem. Geophys. Geosyst.*, *11*, Q04007, doi:10.1029/2009GC002955.
- Carlson, R. L. (2011), The effect of hydrothermal alteration on the seismic structure of the upper oceanic crust: Evidence from Holes 504B and 1256D, *Geochem. Geophys. Geosyst.*, *12*, Q09013, doi:10.1029/2011GC003624.
- Carlson, R. L. (2014), The influence of porosity and crack morphology on seismic velocity and permeability in the upper oceanic crust, *Geochem. Geophys. Geosyst.*, *15*, 10–27, doi:10.1002/2013GC004965.
- Choi, J., and R. P. Lowell (2015), The response of two-phase hydrothermal systems to changing magmatic heat input at mid-ocean ridges, *Deep Sea Res., Part II*, *121*, 17–30, doi:10.1016/j.dsr2.2015.05.005.
- Christensen, N. I. (1996), Poisson's ratio and crustal seismology, *J. Geophys. Res.*, *101*(B2), 3139–3156, doi:10.1029/95JB03446.
- Clague, D. A., B. M. Dreyer, J. B. Paduan, J. F. Martin, D. W. Caress, T. P. Guilderson, and M. L. Mcgann (2014), Eruptive and tectonic history of the Endeavour Segment, Juan de Fuca Ridge, based on AUV mapping data and lava flow ages, *Geochem. Geophys. Geosyst.*, *15*, 3364–3391, doi:10.1002/2014GC005415.
- Delaney, J. R., R. E. McDuff, and J. E. Lupton (1984), Hydrothermal fluid temperatures of 400°C on the Endeavour Segment, northern Juan de Fuca Ridge, *Eos Trans. AGU*, *65*(973), 45.
- Fontaine, F. J., M. Cannat, J. Escartin, and W. C. Crawford (2014), Along-axis hydrothermal flow at the axis of slow spreading Mid-Ocean Ridges: Insights from numerical models of the Lucky Strike vent field (MAR), *Geochem. Geophys. Geosyst.*, *15*, 2918–2931, doi:10.1002/2013GC005162.
- Germanovich, L. N., R. P. Lowell, and P. Ramondenc (2011), Magmatic origin of hydrothermal response to earthquake swarms: Constraints from heat flow and geochemical data, *J. Geophys. Res.*, *116*, B05103, doi:10.1029/2009JB006588.
- Hoof, E. E. E., et al. (2010), A seismic swarm and regional hydrothermal and hydrologic perturbations: The northern Endeavour segment, February 2005, *Geochem. Geophys. Geosyst.*, *11*, Q12015, doi:10.1029/2010GC003264.
- Humphris, S. E., and J. R. Cann (2000), Constraints on the energy and chemical balances of the modern TAG and ancient Cyprus seafloor sulfide deposits, *J. Geophys. Res.*, *105*(B12), 28,477–28,488, doi:10.1029/2000JB900289.
- Kelley, D. S., J. A. Baross, and J. R. Delaney (2002), Volcanoes, fluids, and life at mid-ocean ridge spreading centers, *Annu. Rev. Earth Planet. Sci.*, *30*, 385–491, doi:10.1146/annurev.earth.30.091201.141331.
- Kelley, D., et al. (2012), Endeavour Segment of the Juan de Fuca Ridge: One of the most remarkable places on Earth, *Oceanography*, *25*, 44–61, doi:10.5670/oceanog.2012.03.
- Kellogg, J. (2011), Temporal and spatial variability of hydrothermal fluxes within a mid-ocean ridge segment, PhD thesis, Univ. of Washington, Seattle.
- Kern, H., T. Popp, F. Gorbatshevich, A. Zharikov, K. V. Lobanov, and Y. P. Smirnov (2001), Pressure and temperature dependence of V_p and V_s in rocks from the superdeep well and from surface analogues at Kola and the nature of velocity anisotropy, *Tectonophysics*, *338*(2), 113–134, doi:10.1016/S0040-1951(01)00128-7.
- Liu, L., and R. P. Lowell (2009), Models of hydrothermal heat output from a convecting, crystallizing, replenished magma chamber beneath an oceanic spreading center, *J. Geophys. Res.*, *114*, B02102, doi:10.1029/2008JB005846.
- Lowell, R. P., and L. N. Germanovich (2004), Hydrothermal processes at mid-ocean ridges: Results from scale analysis and single-pass models, *Mid-Ocean Ridges*, 219–244, doi:10.1029/148GM09.
- Lowell, R. P., A. Farough, J. Hoover, and K. Cummings (2013), Characteristics of magma-driven hydrothermal systems at oceanic spreading centers, *Geochem. Geophys. Geosyst.*, *14*, 1756–1770, doi:10.1002/ggge.20109.
- Macdonald, K. C., P. J. Fox, R. T. Alexander, R. Pockalny, and P. Gente (1996), Volcanic growth faults and the origin of Pacific abyssal hills, *Nature*, 125–129.
- Morgan, J., M. Warner, G. Arnoux, E. Hoof, D. Toomey, B. VanderBeek, and W. Wilcock (2016), Next-generation seismic experiments—II: Wide-angle, multi-azimuth, 3-D, full-waveform inversion of sparse field data, *Geophys. J. Int.*, *204*(2), 1342–1363, doi:10.1093/gji/ggv513.
- Singh, S., R. P. Lowell, and K. C. Lewis (2013), Numerical modeling of phase separation at Main Endeavour Field, Juan de Fuca Ridge, *Geochem. Geophys. Geosyst.*, *14*, 4021–4034, doi:10.1002/ggge.20249.
- Singh, S. C., J. S. Collier, A. J. Harding, G. M. Kent, and J. A. Orcutt (1999), Seismic evidence for a hydrothermal layer above the solid roof of the axial magma chamber at the southern East Pacific Rise, *Geology*, *27*(3), 219–222, doi:10.1130/0091-7613(1999)027<0219:SEFAHL>2.3.CO;2.
- Swift, S., M. Reichow, A. Tikku, M. Tominaga, and L. Gilbert (2008), Velocity structure of upper ocean crust at ocean drilling program site 1256, *Geochem. Geophys. Geosyst.*, *9*, Q10013, doi:10.1029/2008GC002188.
- Thompson, W. J., R. E. McDuff, F. R. Stahr, D. R. Yoerger, and M. Jakuba (2005), Heat flux from the Endeavour segment of the Juan de Fuca Ridge, *Eos Trans. AGU*, *86*, Fall Meet. Suppl., Abstract T31A-0489.
- Thurber, C. H. (1983), Earthquake locations and three-dimensional crustal structure in the Coyote Lake Area, central California, *J. Geophys. Res.*, *88*(B10), 8226–8236, doi:10.1029/JB088iB10p08226.
- Toomey, D. R., and G. R. Foulger (1989), Tomographic inversion of local earthquake data from the Hengill-Grensdalur Central Volcano Complex, Iceland, *J. Geophys. Res.*, *94*(B12), 17,497–17,510, doi:10.1029/JB094iB12p17497.
- Toomey, D. R., S. C. Solomon, and G. M. Purdy (1994), Tomographic imaging of the shallow crustal structure of the East Pacific Rise at 9°30′N, *J. Geophys. Res.*, *99*(B12), 24,135–24,157, doi:10.1029/94JB01942.
- Van Ark, E. M., R. S. Detrick, J. P. Canales, S. M. Carbotte, A. J. Harding, G. M. Kent, M. R. Nedimovic, W. S. D. Wilcock, J. B. Diebold, and J. M. Babcock (2007), Seismic structure of the endeavour segment, Juan de Fuca Ridge: Correlations with seismicity and hydrothermal activity, *J. Geophys. Res.*, *112*, B02401, doi:10.1029/2005JB004210.
- Warner, M., et al. (2013), Anisotropic 3D full-waveform inversion, *Geophysics*, *78*(2), R59–R80, doi:10.1190/geo2012-0338.1.
- Weekly, R. T., W. S. D. Wilcock, E. E. Hoof, D. R. Toomey, P. R. McGill, and D. S. Stakes (2013), Termination of a 6 year ridge-spreading event observed using a seafloor seismic network on the Endeavour Segment, Juan de Fuca Ridge, *Geochem. Geophys. Geosyst.*, *14*, 1375–1398, doi:10.1002/ggge.20105.

- Weekly, R. T., W. S. D. Wilcock, D. R. Toomey, E. E. E. Hooft, and E. Kim (2014), Upper crustal seismic structure of the Endeavour segment, Juan de Fuca Ridge from travelttime tomography: Implications for oceanic crustal accretion, *Geochem. Geophys. Geosyst.*, *15*, 1296–1315, doi:10.1002/2013GC005159.
- Wilcock, W. S. D., and J. R. Delaney (1996), Mid-ocean ridge sulfide deposits: Evidence for heat extraction from magma chambers or cracking fronts?, *Earth Planet. Sci. Lett.*, *145*(1–4), 49–64, doi:10.1016/S0012-821X(96)00195-1.
- Wilcock, W. S. D., E. E. E. Hooft, D. R. Toomey, P. R. McGill, A. H. Barclay, D. S. Stakes, and T. M. Ramirez (2009), The role of magma injection in localizing black-smoker activity, *Nat. Geosci.*, *2*, 509–513, doi:10.1038/ngeo550.